Mechanistic and Experimental Aspects of the Structural Characterization of Some Model and Real Systems by Nitrogen Sorption and Mercury Porosimetry

Carlos Felipe, Fernando Rojas, Isaac Kornhauser, Matthias Thommes and Giorgio Zgrablich

Reprinted from

Adsorption Science & Technology

2006 Volume 24 Number 8

Multi-Science Publishing Co. Ltd.
5 Wates Way, Brentwood, Essex CM15 9TB, United Kingdom

Mechanistic and Experimental Aspects of the Structural Characterization of Some Model and Real Systems by Nitrogen Sorption and Mercury Porosimetry†

Carlos Felipe[1,2], Fernando Rojas[1*], Isaac Kornhauser[1], Matthias Thommes[3] and Giorgio Zgrablich[4] *(1) Departamento de Química, Universidad Autónoma Metropolitana-Iztapalapa, P.O. Box 55-534, México D.F. 09340, México. (2) Departamento de Fisicoquímica de Materiales, Instituto de Ciencias, Benemérita Universidad Autónoma de Puebla, Puebla 72000, México. (3) Quantachrome Instruments, 1900 Corporate Drive, Boynton Beach, FL 33426, U.S.A. (4) Laboratorio de Ciencias de Superficies y Medios Porosos, Universidad Nacional de San Luis, San Luis 5400, Argentina.*

(Received 21 June 2006; revised form accepted 13 November 2006)

ABSTRACT: Several mechanistic and phenomenological aspects of mercury intrusion and nitrogen sorption processes involving some model and real mesoporous systems were studied. The experimental pore systems examined consisted of two substrates: (a) a globular solid composed of monodisperse silica spheres in a perfect rhombohedral arrangement and (b) a controlled pore glass solid. Comparisons between the experimental nitrogen sorption and mercury porosimetry pore-size distributions demonstrated: (i) the existence of several mechanistic effects responsible of irreversible capillary behaviour that influences the calculation of pore structure parameters; (ii) the choice of the right sorption process (i.e. condensation or evaporation) suitable for comparison with either intrusion or extrusion results; (iii) the types of porous structures capable of convenient pore-size characterization by either nitrogen sorption and/or mercury porosimetry methods; and (iv) the nature of the pore entities (i.e. chambers or necks) that control the incumbent capillary process.

1. INTRODUCTION

A long-standing aim (Scherer 1998; Rigby 2000), inherent to the characterization of a given porous material, has been to try to reconcile the pore structural parameters (e.g. pore-size distribution, surface area, porosity, etc.) determined from adsorption/desorption experiments and those obtained from intrusion/extrusion measurements. An assessment of this kind often highlights important discrepancies between the two sets of results, with much of this disagreement arising from two main reasons:

— an inappropriate choice of a prototype for the porous material which most resembles a real sample. This choice is associated with both: (i) the visualization of porous materials as being composed of independent or interconnected pore domains (Figure 1) and (ii) the geometrical (morphological) characteristics of the void entities comprising the sample;

†On the occasion of the 10th anniversary of the deaths of our late friends and outstanding capillary scientists John Michael Haynes (Bristol, U.K.) and Vicente Mayagoitia (México).

*Author to whom all correspondence should be addressed. E-mail: fernando@xanum.uam.mx.

— the emergence of irreversible or hysteresis phenomena during adsorption/desorption and intrusion/extrusion processes.

At present, it can be presumed with a fair certainty that the following capillary effects cause irreversible behaviour when vapour sorption occurs inside interconnected porous networks:

— *advanced adsorption* (Esparza *et al*. 2004) (or advanced liquid-filling), in which some tubular capillaries are filled at vapour pressures lower than those required if these pores existed as isolated entities (i.e. disconnected from other pores). This happens by the intrusion of a liquid–vapour interface (i.e. a liquid front moving from a neighbouring cavity) into the capillary in question;
— *delayed adsorption* (Sing 1998), in which chambers inside an interconnected pore network are filled with condensate at vapour pressures higher than those required if these same cavities acted as isolated pores. This happens as a result of the requirement to first establish a continuous liquid–vapour interface inside an initially empty cavity (through filling of its surrounding throats with condensate) before this meniscus can advance and eventually collapse towards the centre of the cavity in order to replenish it completely with condensate;
— *cavitation* (Sarkisov and Monson 2001) [or the *tensile strength* effect (Everett 1967)], i.e. the spontaneous nucleation of vapour bubbles in the condensate phase residing in the pores as the pressure drop across the liquid–vapour interface becomes sufficiently high.

In turn, during intrusion/extrusion operations, the following phenomena can arise:

— *contact angle hysteresis* (Salmas and Androutsopoulos 2001; Lam *et al*. 2001), a phenomenon in which the advancing (intrusion) and retraction (extrusion) contact angles differ from each other;
— *canthotaxis* (Martinez *et al*. 1987; Domingues Dos Santos and Ondarc 1996), an effect occurring during an intrusion (or extrusion) operation when the liquid–vapour interface anchors itself to a pore-to-pore edge until it acquires an adequate curvature to start penetrating the void ahead (Figure 2);
— *liquid-phase entrapment* (Tsakiroglou *et al*. 1997), which arise during an extrusion operation when the receding liquid phase loses its connection to the outer source phase. This usually happens through the snap-off of liquid threads at some capillary passages inside the porous network.

The existence of metastable meniscus shapes and/or of cooperative phenomena during the course of a capillary process leads to the emergence of hysteresis (Everett 1967), with *pore hysteresis* and *network hysteresis* being the contributors to this phenomenon most recognized. Consideration of the whole set of interactions existing among molecules in an adsorption system (Broekhoff and de Boer 1967; Ravikovitch *et al*. 1998), i.e. solid–fluid and fluid–fluid contributions, has proved to be essential in the identification of stable and metastable menisci shapes and for predicting the precise conditions at which a phase transition is taking place during the development of a capillary phenomenon in a mesoporous entity.

The following scheme has been followed in the present work with the objective of critically assessing the pore-size distributions arising from both mercury porosimetry and nitrogen sorption experiments in the case of model porous substrates. Firstly, some important mechanistic aspects of intrusion, extrusion and sorption phenomena, as well as explanations of the canthotaxis phenomenon and the effect of the pore-wall orientation on the determination of the pore-size distribution, are provided. Then nitrogen sorption and mercury porosimetry

experiments are employed to characterize two model systems corresponding to extreme cases of porous solids. These systems are: (i) a globular solid comprised of spherical (mono-sized) SiO_2 particles in a regular arrangement, in which pores mostly act as independent domains and (ii) a controlled pore glass constituted of channels formed by alternate necks and bulges. Finally, a discussion of the pore-size distribution results obtained from the two techniques is given in terms of the morphology of each porous medium and the capillary processes taking place therein.

2. MECHANISTIC ASPECTS OF MERCURY INTRUSION/EXTRUSION AND NITROGEN SORPTION

2.1. Mercury penetration

Mercury intrusion is widely used for assessing the pore-size distribution function (PSD) of porous substrates. This technique has been utilized since 1945 subsequent to the work of Ritter and Drake who employed an equation derived previously by Washburn (1921) relating to the penetration of cylindrical capillaries by mercury. Mercury intrusion along a cylindrical pore of radius R_B occurs completely once the liquid (l)–vapour (v) interface penetrates the pore entrance. The pressure P (that becomes equal to the liquid pressure P^l when the vapour pressure is negligible, i.e. $P^v \sim 0$) required to permeate a cylindrical capillary is given by the Young–Laplace equation (Adamson 1990):

$$P^l = -\frac{2\sigma^{lv}\cos\theta}{R_B} = \frac{2\sigma^{lv}}{R_m} = \sigma^{lv}C^{lv} \tag{1}$$

where σ^{lv} is the l–v interfacial tension, R_m and C^{lv} are the radius of curvature and curvature of the l–v interface, respectively, and θ is the contact angle at the three-phase line of contact.

In contrast to the penetration mechanism exhibited by cylindrical pores, mercury intrusion inside a spherical pore follows a different pattern (Cebeci 1980; de Botton 1985). If it is assumed that the spherical cavity has direct access to mercury (e.g. through a cylindrical capillary of radius R_B directly connected to it) and if the equilibrium contact angle θ between the l–v interface and the pore wall is attained at all times, then the pressure P^l necessary to invade the cavity is given by:

$$P^l = -\frac{2\sigma^{lv}\cos\Phi}{R_B} \tag{2}$$

In this equation, Φ ($= \theta + \alpha$), is the angle formed between the pore axis (x-axis), which is assumed to be parallel to the walls at the pore entrance and the line which is tangential to the l–v interface at the point at which the three-phase line of contact is anchored (see Figure 2), and α is the angle of inclination of the spherical pore wall (with respect to the pore axis) at the entrance point. The quantity α can also be expressed in terms of the radius of the spherical cavity, R_S, and the radius of the bond, R_B, that gives access to the site:

$$\alpha = \tan^{-1}\left(\frac{R_S^2}{R_B^2} - 1\right)^{1/2} \tag{3}$$

It should be noted that once the meniscus overcomes the bond-site entrance, the cavity starts to be filled completely with liquid as long as the l–v interface maintains its equilibrium contact angle θ with the spherical wall on which the displacement is now occurring. This situation corresponds to an *unstable* Laplace process (Everett and Haynes 1975) by virtue of the following inequality:

$$\frac{dV^l}{dC^{lv}} \propto \frac{dV^l}{dP^l} < 0 \quad (\therefore \text{ unstable Laplace process}) \tag{4}$$

Conversely, a *stable* Laplace process would occur if:

$$\frac{dV^l}{dC^{lv}} \propto \frac{dV^l}{dP^l} \geq 0 \quad (\therefore \text{ stable Laplace process}) \tag{5}$$

2.2. Canthotaxis phenomena during mercury intrusion into interconnected pore networks

A cavity (site) in a porous network can be invaded by mercury through any of its surrounding C throats (bonds) (Figure 1), provided that this latter capillary is linked to the external mercury supply through a continuous liquid path. In addition to this condition, the l–v meniscus should be capable of overcoming a pressure barrier existing at the bond-site edge [i.e. a *canthotaxis* or "anchoring-at-an-edge" effect (de Botton 1985)] in order to occupy the chamber; the height of this barrier being greater the smaller the ratio between the radius of the bond (R_B) and the radius of the site (R_S). If a bond connected to a site is just intruded by mercury in such a way that the current radius of curvature of the l–v interface at the site entrance is $R_{B,0}/|\cos\theta|$, then two situations can emerge (Figure 2):

— If $R_{B,0}/R_S \geq |\cos\theta|$, the l–v meniscus first anchors at the pore-to-pore edge (i.e. a phenomenon called *canthotaxis* emerges) while its radius of curvature starts to decrease from $R_{B,0}/|\cos\theta|$ down to $R_{B,0}/|\cos\Phi|$ as P^l increases. This latter radius of curvature represents the onset of complete filling of the site, since this state now corresponds to an unstable Laplace situation [Figure 2(b); $0 \leq \alpha \leq \pi - \theta$; $\theta \leq \Phi \leq \pi$].

— If $R_{B,0}/R_S < |\cos\theta|$, the mercury meniscus again anchors at the bond-site edges but this time undergoes a more intense canthotaxis, starting to increase its curvature (and similarly P^l) up to the maximum value associated with a mean radius of curvature $R_m = R_{B,0}$, at which point the site is completely intruded by mercury [Figure 2(a); $\alpha > \pi - \theta$, $\Phi > \pi$].

The situations described above can be summarized as follows. For a meniscus to invade a site irreversibly, it should first establish (at the bond-site entrance) its equilibrium contact angle with the spherical pore walls into which intrusion will occur. This involves a decrease in its radius of curvature from $R_{B,0}/|\cos\theta|$ down to $R_{B,0}/|\cos\Phi|$; in other words, P^l has to increase up to a threshold value. This is equivalent to saying that, when $R_{B,0}/R_S \geq |\cos\theta|$, the meniscus first anchors at the bond-site edge and then starts to increase continuously (as P^l increases) until it reaches a limiting radius of curvature, at which point its irreversible displacement into the cavity occurs. On the other hand, when $R_{B,0}/R_S < |\cos\theta|$, the meniscus is again anchored at the bond-site edge, but this time starts to increase up to the highest (maximum) possible P^l pressure (i.e. that

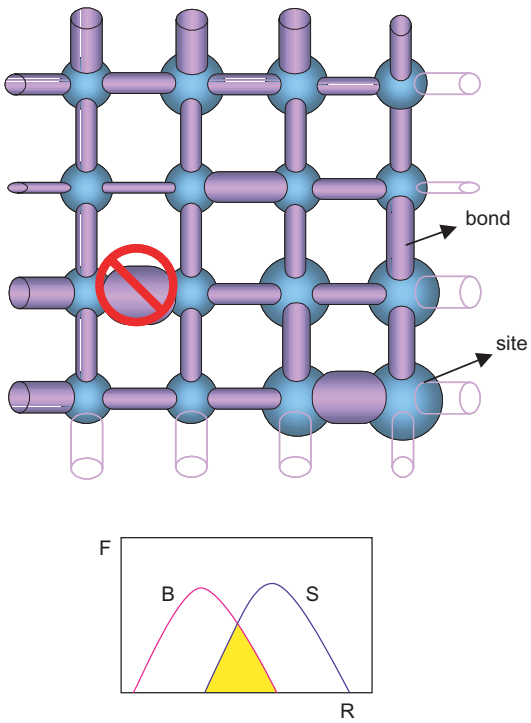

Figure 1. (Upper part): Description of sites (cavities, hollow spheres) and bonds (throats, hollow cylinders). Bonds larger than sites (see that associated with the symbol ⊘) are not permissible in a consistent porous network. (Lower part): Overlap between site (F_S) and bond (F_B) size distributions.

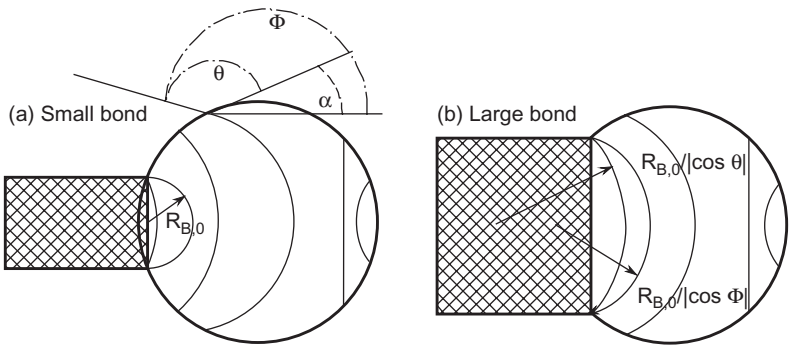

Figure 2. Advancing menisci during mercury intrusion from a contiguous bond into a spherical site, with the canthotaxis phenomenon being shown as occurring at a pore-to-pore edge. Breakthrough intrusion in a given site from: (a) a small bond requires that the l–v meniscus attains a radius of curvature $R_{B,0}$; (b) a large bond demands that the radius of curvature of the interface becomes $R_{B,0}/|\cos\Phi|$.

corresponding to a radius of curvature equal to $R_{B,0}$). The site is then completely flooded with mercury through the spontaneous displacement of the l–v interface (i.e. an unstable Laplace process commences from this point onwards since $dV^1 / dP^1 < 0$).

The whole set of above observations may be summarized in terms of the pressure P^{l} necessary to allow the complete intrusion of mercury into a spherical site of radius R_S from a cylindrical bond of radius $R_{B,0}$:

$$P^{l} = \begin{cases} \dfrac{2\sigma}{R_{B,0}} & \text{if} \quad R_{B,0} \le R_s|\cos\theta| \\ -\dfrac{2\sigma}{R_{B,0}}\cos\left[\tan^{-1}\left(\dfrac{R_S^2}{R_{B,0}^2}-1\right)^{0.5} + \theta\right] & \text{if} \quad R_{B,0} > R_s|\cos\theta| \end{cases} \tag{6}$$

For a porous network, mercury intrusion is usually recognized as being mainly controlled by bonds rather than sites because of the smaller sizes assumed by the former void elements. The critical radius of curvature, R_C, required for an l–v meniscus to completely invade a bond of radius R is given by equation (1). Nevertheless, for an initially empty bond to be permeated by mercury from any one of its two ends, the existence (at its other end) of a continuum liquid path leading to the outer mercury bulk source is also required.

2.3. Mercury intrusion/extrusion in a tubular capillary of varying cross-section

Some mechanistic aspects pertinent to mercury penetration and extrusion processes that occur inside tubular pores of varying cross-section (Cebeci 1980; Reyes-de la Cruz 1979) can shed light upon the interpretation of pore-size results obtained for pore networks consisting of alternating wide and narrow hollow sections. To illustrate the mechanistic aspects that we wish to highlight, let us assume that mercury intrusion and extrusion take place in a sinusoidal pore such as that shown in Figure 3. On a three-dimensional basis, the pore arrangement can then be thought to be constituted by bulges (region A in Figure 3) and throats (regions B and B' in Figure 3).

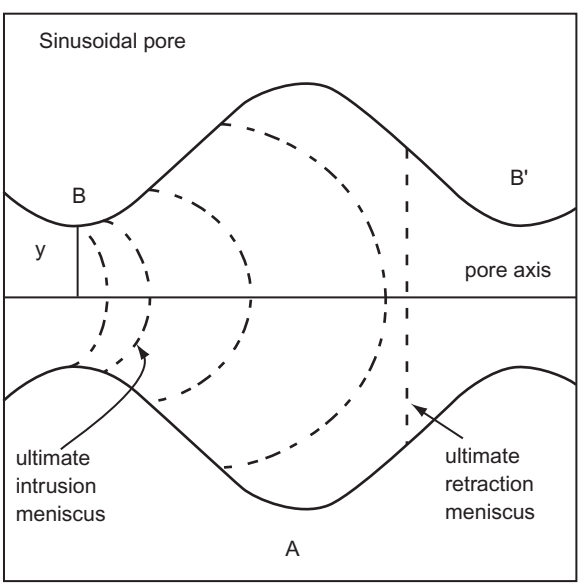

Figure 3. Evolution of menisci during mercury intrusion/extrusion inside a sinusoidal capillary.

Let us now start by describing mercury intrusion into this sinusoidal pore (the bulk mercury phase is assumed to be located at the left-hand side of the pore entrance) and presume that the non-wetting fluid is being forced to enter through the pore mouth B via the application of an appropriate pressure; besides these requirements, the only additional conditions are for the mercury meniscus to be hemispherical and to establish a fixed contact angle θ at the three-phase line of contact. In a similar manner to the process of mercury intrusion into a spherical void, the penetration of mercury into this sinusoidal pore may be described by the same modified Washburn equation [cf. equation (2)] that takes into account not only the contact angle but also the inclination of the pore walls:

$$P^{I} = -\frac{2\sigma^{lv}\cos\Phi}{y} \tag{7}$$

Here, y represents the pore half-width (measured from the pore axis) existing at a certain point (x, y) on the surface of the pore (Figure 3) and $\Phi = \theta + \alpha$. The sequence of menisci progress can be seen in Figure 3. Although one may think that the maximum pressure necessary to completely intrude the pore with mercury is associated with the width of its narrowest cross-section, this is not the case. Instead, and depending on the ratio between the widths of the pore bulge and the pore throat, penetration occurs at a point somewhat beyond the narrowest entrance to the pore, and for which $\alpha > 0$. For a pore of sinusoidal shape, penetration occurs at a pressure larger than that necessary for intrusion into a cylindrical void with the same radius as that of the narrowest pore cross-section of the sinusoidal void. This latter effect becomes more extreme the larger the disparity between the widths of the pore mouth and of the pore bulge. The position of the ultimate stable meniscus, prior to the irreversible trespassing of the whole pore with mercury, is shown in Figure 3.

Now let us proceed with the retraction mechanism. In order to simplify things, let us assume that initially the sinusoidal pore is completely filled with and directly connected to the outer bulk mercury source. The menisci sequence (assuming once more a fixed contact angle at the three-phase line of contact and a hemispherical meniscus shape) can be seen in Figure 3. The ultimate stable meniscus, before liquid is displaced from the pore, occurs at a particular point as depicted in Figure 3. The important point to realize here is that retraction occurs at a particular value $\alpha < 0$, at which point mercury recedes irreversibly until it is completely removed out of the pore element. When the pore amplitude is sufficiently large (i.e. when the narrowest cross-section of the pore differs significantly from the widest one), it is possible that a flat interface or even a meniscus of negative curvature (the centre of curvature lying on the vapour phase side) could be formed, thus making mercury extrusion from an oscillating pore impossible to accomplish. Entrapment of mercury can, therefore, occur in this type of pore.

In conclusion, two important points may be associated with the simulation of mercury intrusion and retraction inside a sinusoidal pore: (i) if one assumes a given non-wetting contact angle, i.e. $90° < \theta < 180°$, then mercury intrusion will occur at some value of $\Phi > \theta$, whilst (ii) partial (rather than total) mercury retraction may occur at some value of $\Phi < \theta$. These two points will be employed later in attempting to explain the qualitative mercury intrusion/extrusion characteristics of one of our model pore systems.

2.4. Nitrogen sorption

Determination of the PSD function from sorption data has been undertaken traditionally via the BJH (Barrett *et al*. 1951) method. Nowadays, new approaches such as the Non-Local Density

Functional Theory (NLDFT) (Ravikovitch *et al*. 1998; Ravikovitch and Neimark 2001, 2002; Neimark and Ravikovitch 2001, 2003) or Grand Canonical Monte Carlo (GCMC) (Gelb and Gubbins 2000a,b) methods are available. These enable improved PSD determinations to be obtained from the deconvolution of experimental sorption results in terms of theoretical isotherms corresponding to pores of the same nature and geometry but of varied sizes. The comparison of results arising from classical, macroscopic methods and modern, microscopic methods of PSD analysis clearly reveals that, in order to describe correctly adsorption in narrow meso-/micro-pores, it is necessary to apply methods based on statistical mechanics which are capable of describing the configuration of adsorbed species at a molecular level. Model porous systems, such as those consisting of a collection of individual non-intersecting cylindrical mesopores [e.g. SBA-15 substrates (Zhao *et al*. 1998a,b)] which depict mere pore hysteresis, have been very useful in deciphering a problem that has remained unresolved for a long time, i.e. the apparent disagreement between the PSD results arising from the adsorption boundary (AB) and desorption boundary (DB) curves of the sorption isotherm (Ojeda *et al*. 2003; Lukens *et al*. 1999).

Sorption hysteresis can be regarded as an intrinsic property of a phase transition (i.e. pore condensation) taking place inside a single, idealized pore which reflects the existence of metastable vapour states associated with the nucleation of the liquid phase (spinoidal condensation). In consequence, condensation could be delayed. On the other hand, assuming a pore of finite length (which is always the case in real adsorbents), vaporization could occur via a receding meniscus. This is a nucleation problem and therefore metastability would not be expected to occur during desorption (evaporation). Within this picture, the experimental desorption branch is often associated with the equilibrium liquid–vapour transition (this equilibrium transition corresponds to the condition at which the two states have the same grand potential), whereas the condensation step corresponds to the spinodal spontaneous transition. Accordingly, the conventional NLDFT approach, which is based on describing the adsorption and phase behaviour of fluids under equilibrium conditions, can be used to extract the pore-size values from the desorption branch of the hysteresis loop (Ravikovitch *et al*. 1998; Ravikovitch and Neimark 2001). On the other hand, the so-called NLDFT metastable adsorption branch kernel developed by Neimark and Ravikovitch (2001) provides a correct description of the position of the pore condensation threshold (i.e. the conditions at which the spinodal condensation occurs) by taking into account the pressure range at which a metastable pore fluid can exist prior to condensation. Hence, the application of this NLDFT-AB (adsorption branch) kernel also enables the correct pore-size distribution curve to be obtained from the AB isotherm (Neimark and Ravikovitch 2001). This is important when the material under analysis consists of a network of ink-bottle type pores where percolation effects are expected to have a significant influence on the position of the desorption branch of the hysteresis loop.

Where pore blocking/percolation and cavitation effects do not contribute to hysteresis, the PSD curves obtained from the adsorption and desorption branches should coincide (of course it is important to make sure that the pore geometry assumed in the NLDFT kernel agrees principally with the pore geometry of the pores in the adsorbent). If the results do not agree, it may be concluded that: (i) the adsorbent cannot be modelled as an assembly of independent pores; or (ii) the adsorption experiment was not performed correctly (artificial wide hysteresis loops are observed if adsorption/desorption experiments are not carried out under equilibrium conditions). Here, we have used both types of NLDFT kernels (AB and DB) to calculate the PSD functions inherent to an SiO_2-CPG sample (see Section 4 below).

During the sorption experiments employed to perform PSD determinations, irreversible capillary condensation effects are frequently found and concomitant filling or emptying effects

may occur (Mayagoitia 1993). On the one hand, a site or chamber might be filled with *delay* (Mayagoitia *et al*. 1985) during condensate uptake due to the necessary requirement that a continuous l–v interface should exist around its surface before this meniscus can move towards the centre of the cavity. During the occurrence of a phase transition, the presence of some empty bonds around the site can cause a discontinuity at the l–v interface. On the other hand, it is possible that when a site or bulge is occupied by liquid the advancing interface can subsequently invade the next empty bond linked to this site, thus filling it completely with condensate (Mayagoitia *et al*. 1985). This kind of filling process occurs at a relative vapour pressure lower than that required for the condensation of liquid in a lone, independent capillary. Hence, on the basis of the above discussion, *advanced adsorption* (Esparza *et al*. 2004) is appropriate for bonds while *delayed adsorption* (Mayagoitia *et al*. 1985) is associated with sites.

Let us now consider a hollow tube of varying cross-section [Figure 4(a)] and imagine that capillary condensation is first taking place at the pair of narrow necks (B and B') that are delimiting a bulge (A) (Everett 1975). This creates an l–v meniscus around A that can advance either immediately or at a later stage of the uptake process into the bulge, filling it completely with

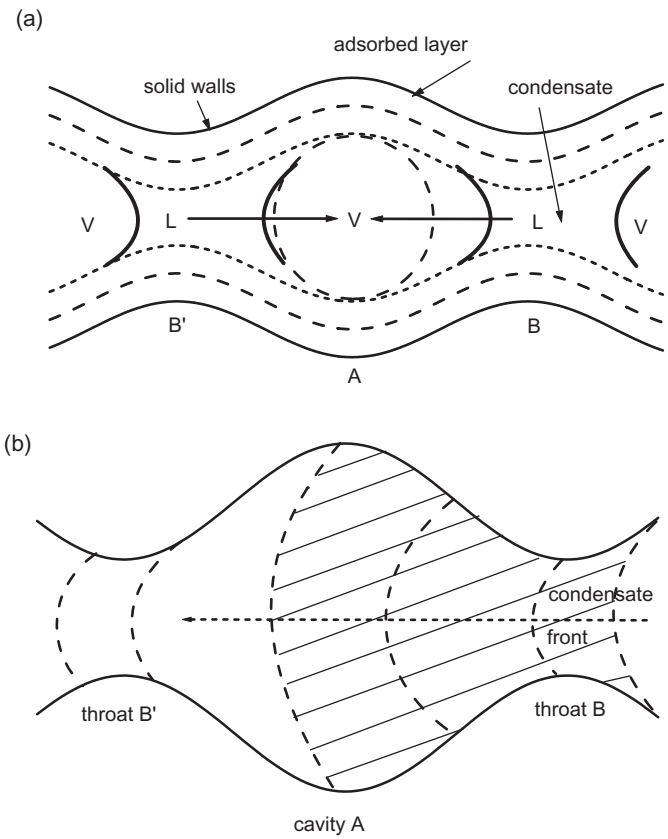

Figure 4. Configuration of menisci during capillary condensation in a tubular pore of varying cross-section. Two cases are depicted: (a) that in which capillary condensation first occurs at neighbouring bonds and afterwards at the site in between these two necks; (b) that in which an advancing l–v meniscus first induced at one bond (B) starts bypassing the neighbouring cavity (A) and (subsequently) the next adjacent bond (B').

condensate. Let us now assume that necks B and B' can be approximated as cylinders of radii R_B and $R_{B'}$, respectively, and that the cavity is a spherical hollow of radius R_S. In terms of the classical Kelvin equation and assuming that $R_B < R_S/2 \cap R_{B'} < R_{S'}/2$, filling of the cavity should follow once these two necks are already occupied by condensate. Nonetheless, a second possibility can also arise when any one of the two necks surrounding the cavity is already filled by condensate. In this case, an advancing meniscus can completely bypass the chamber in question provided that $R_B \geq R_S/2$ [Figure 4(b)]. The movement of the latter meniscus can probably continue into the next throat, thereby invading it completely with condensate. The movement of the meniscus can even continue throughout further void elements located beyond the bond–site–bond sequence considered above.

3. EXPERIMENTAL

Nitrogen sorption isotherms were measured at 76 K (boiling point of nitrogen at Mexico City's 2200 m altitude) in an automatic Quantachrome Autosorb-1 instrument. Samples were outgassed under vacuum overnight at 473 K in a turbomolecular pump system. Mercury intrusion/extrusion curves were determined by means of a Quantachrome Dual Pore Master instrument. The model pore systems that were selected to perform this work were the following:

— a Stanpore silica sample consisting of monodisperse SiO_2 spheres with a nominal diameter of 200 nm packed in a rhombohedral arrangement, i.e. in accordance with a coordination number of 12, as obtained from Louis Schleiffer AG, Zurich, Switzerland. The nominal total pore volume of the Stanpore sample was 160 mm^3/g.
— a controlled pore glass (CPG) reference material as obtained from The Federal Institute for Materials Research and Testing (BAM, Germany) via Quantachrome. These porous glass beads constitute a certified reference material for mercury intrusion designated as CRM BAM-PM-121*.

4. RESULTS AND DISCUSSION

4.1. Stanpore SiO_2 solid

The SEM micrographs depicted in Figure 5 show the lattice packing of the Stanpore SiO_2 sample composed of monodisperse quasi-spherical particles of 245 nm diameter arranged in a rhombohedral fashion (Graton and Fraser 1935). The corresponding nitrogen sorption isotherm and mercury intrusion/extrusion curves are depicted in Figures 6 and 7, respectively. The pore structure of this class of aggregates contains of two kinds of holes, i.e. *tetrahedral* and *octahedral* cavities both delimited by triangular foramina (Graton and Fraser 1935). The diameters that fit the octahedral, tetrahedral and triangular holes of this regular array of spheres of radius R correspond to 0.414R, 0.225R and 0.155R, respectively. According to the IUPAC classification (Sing *et al*. 1985), the nitrogen isotherm of the Stanpore silica sample depicts a type H1 hysteresis loop. The AB section of the isotherm exhibits quite a steep slope over the relative vapour pressure interval $P/P^0 \in [0.965, 0.99]$; similarly, the DB curve (as well as the primary scanning desorption curves) depicts a percolation threshold at ca. $P/P^0 = 0.965$.

*http://www.bam.de/pdf/service/referenzmaterialien/zertifikate/phys_eigenschaften/bam_pm_121.pdf.

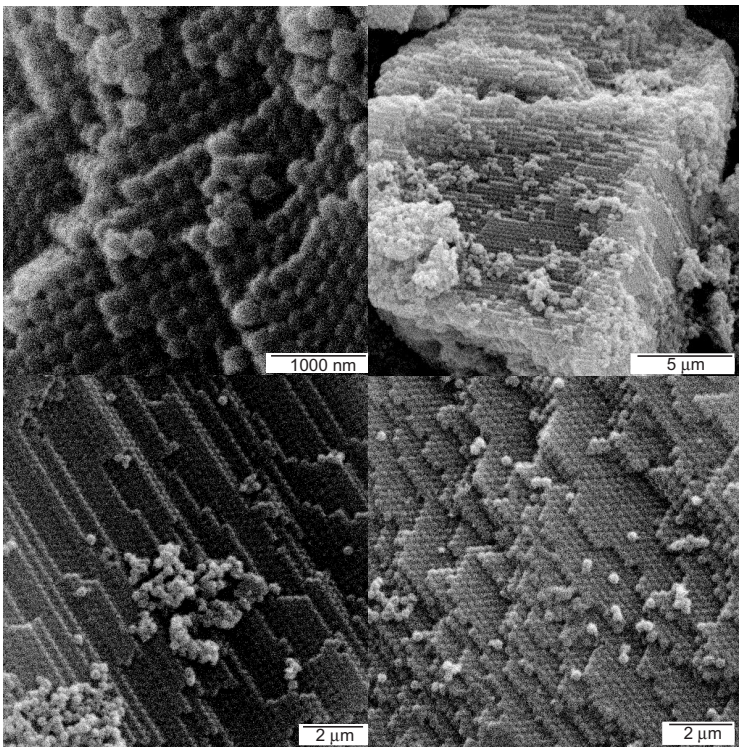

Figure 5. SEM images illustrating the lattice packing of Stanpore silica.

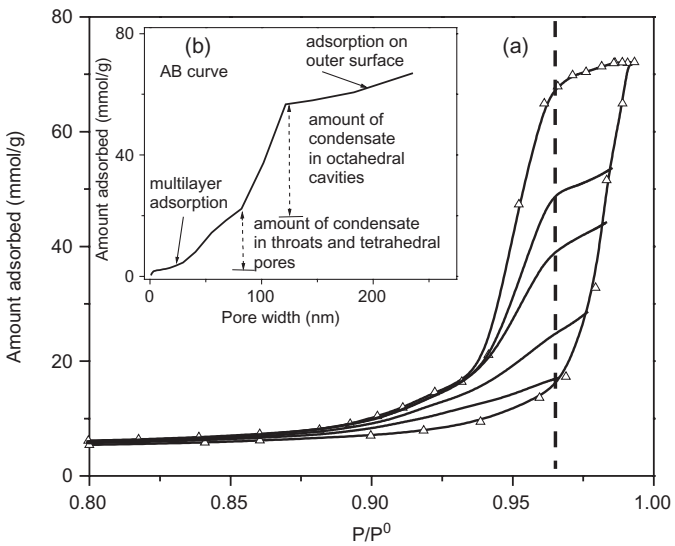

Figure 6. (a) Nitrogen sorption isotherm measured at 76 K on Stanpore silica. The vertical dashed line marks the onset of vapour percolation. (b) Qualitative aspects of the sequential filling of the pores associated with the rhombohedral packing of Stanpore silica.

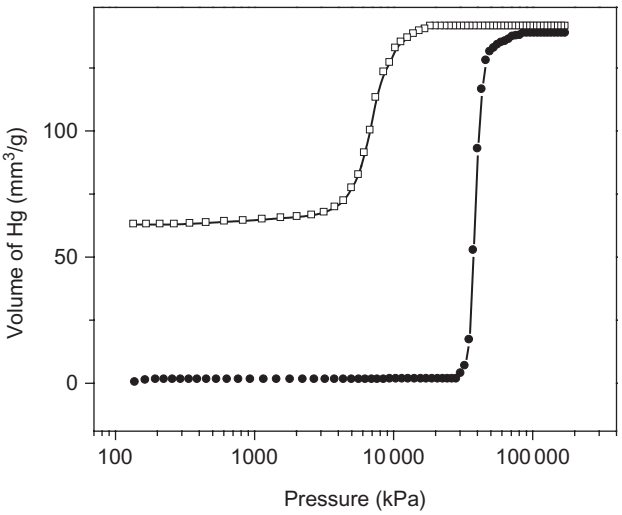

Figure 7. Mercury intrusion (●)/extrusion (□) curves for Stanpore silica.

The values for some of the pore network structural parameters of Stanpore silica are reported in Table 1. The porosity of the arrangement measured by nitrogen sorption and mercury intrusion corresponded to 0.247 and 0.238, respectively. These values show good agreement with the theoretical value of 0.2595; the small difference can be attributed to some deformation existing between neighbouring globules at the point of contact and the existence of a few macropores.

Realizations reported previously (Aristov *et al*. 1962) indicate that (i) the tetrahedral cavities of a rhombohedral packing of equal spheres are filled with condensate concurrently with condensation at their surrounding triangular necks, and (ii) octahedral holes fill with condensate at higher pressures once all throats (and consequently all tetrahedral pores) are initially filled with condensate. Additionally, one can re-create the sequence of filling of the pores that constitute a rhombohedral arrangement by plotting the nitrogen AB isotherm as the amount adsorbed versus the pore width (this latter value being calculated using the BJH procedure) [see Figure 6(b)]. This latter plot allows a quite distinct identification of the pore-filling processes described above. In

TABLE 1. Pore Structural Properties of Stanpore Silica[a]

ε_{N_2}	ε_{Hg}	A_{BET} (m^2/g)	A_t (m^2/g)	A_{Hg} (m^2/g)	$V^P_{N_2}$ (mm^3/g)	V^P_{Hg} (mm^3/g)	R_{sph} (nm)	AB-PSD modes (nm)	DB-PSD mode (nm)	Hg-intr PSD modes (nm)
0.247	0.238	12.6	11.5	15.0	149	142	245	101.6, 49.5	38.6	37.5, 49.5

[a]ε_{N_2} = porosity from nitrogen sorption; ε_{Hg} = porosity from mercury intrusion; A_{BET} = BET surface area; A_t = t surface area; A_{Hg} = surface area from mercury intrusion; $V^p_{N_2}$ = pore volume from nitrogen sorption; V^p_{Hg} = pore volume from mercury intrusion; R_{sph} = mean radius of globules (TEM).

Figure 6(b), the condensed volume existing inside the octahedral pores corresponded to ca. 73% of the total liquid volume retained in all the pores, while the condensate located inside the tetrahedral pores amounted to 27% of the total volume. These values are in very good agreement with the nominal pore volumes of a rhombohedral packing, viz. 71.7% for octahedral holes and 28.3% for tetrahedral holes. Hence, the quantitative filling aspects depicted in Figure 6(b) are likely to be correct. In turn, the mercury porosimetry analysis (Figure 7) indicates that 45% of the total intruded volume remained trapped inside the Stanpore sample after completion of the retraction process. This means that mercury can recede not only from tetrahedral pores but also from a number of octahedral ones; snap-off (Rigby 2000) occurring at pore entrances delimiting some of the former cavities provides a likely reason for the inability of mercury menisci to intrude into many of these octahedral pores.

The PSDs determined from mercury intrusion and nitrogen sorption are depicted in Figure 8. The intrusion curve has been analyzed via the Washburn equation assuming a contact angle $\theta = 140°$; in turn, the BJH method has been employed to evaluate the nitrogen PSD since, for large mesopores such as those existing in the Stanpore sample, the results obtained by this method have a high confidence limit (Ravikovitch *et al*. 1998; Ravikovitch and Neimark 2001, 2002; Neimark and Ravikovitch 2001, 2003; Gelb and Gubbins 2000a,b). Additionally, the following comments are pertinent:

— The BJH-PSD modes of octahedral pores and triangular necks calculated from nitrogen sorption were 101.6 nm (AB curve) and 38.6 nm (DB curve), respectively (Figure 8 and Table 1). The sizes of ideal octahedral holes and triangular throats are $0.414 \times 245 \approx 101$ nm and $0.155 \times 245 \approx 38$ nm, respectively, thus confirming that the Stanpore sample involved a quite regular rhombohedral packing of monodisperse spherical globules. A second and shallower (i.e. extended) AB-BJH-PSD mode peak appeared at ca. 49.5 nm, probably resulting from condensate filling of the triangular throats and tetrahedral holes in the Stanpore sample (i.e. the expected in-sphere diameter of tetrahedral pores corresponds to $0.225 \times 245 \approx 55$ nm).

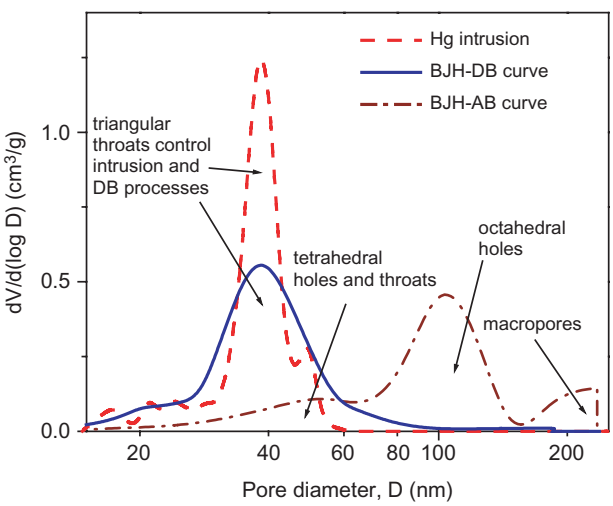

Figure 8. Mercury intrusion and BJH pore-size distributions of Stanpore silica.

— The mercury-intrusion branch yields PSD mode values of 37.5 (sharp) and 49.5 (shallow) nm, respectively (Figure 8). The first value is close to the sharpest peak of the N_2-DB-BJH-PSD while the second one closely resembles the shallow peak of the AB-BJH-PSD curve. These results indicate that the triangular throats control both nitrogen desorption and mercury intrusion phenomena. In contrast, the N_2-AB-BJH-PSD result gave appreciably larger pore sizes as well as a wider distribution. Again, this indicates that octahedral voids are filled with condensate after their surrounding throats, while tetrahedral pores are filled together with bonds.
— Since bond sizes are significantly smaller than octahedral sites, the porous structure corresponds to a type II arrangement according to the DSBM classification (Mayagoitia 1993). This structural assignment is supported by the twin-peak appearance of the AB-PSD that allows a clear discrimination between throats and octahedral cavities.
— A rather similar percolation threshold at ca. $P/P^0 = 0.965$ is displayed by the DB curve as well as by the set of primary descending scanning (PDS) isotherms (see the vertical dashed line in Figure 6). This indicates that a sudden desorption from either a saturation state or from a partially saturated state occurs when throats start expelling condensate, thereby provoking the percolative and simultaneous emptying of tetrahedral and octahedral cavities.

4.2. Controlled pore glass (CPG)

4.2.1. Nitrogen sorption

Electron microscopy revealed that the structure of CPG is in reality a three-dimensional network of interconnected channels (see inset in Figure 9), each being a sinuous path of alternating throats and bulges. From the work of Cross and Haynes (1973), it can be suggested that, because of the fluid state adopted by borosilicate glasses during their thermal phase separation, the interface between the B_2O_3- and SiO_2-rich phases adopts a constant, anticlastic curvature. Nevertheless, as

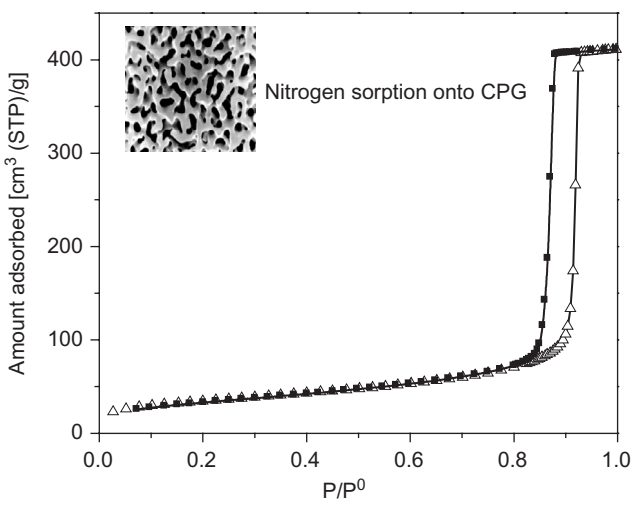

Figure 9. Nitrogen sorption isotherm at 76 K on the CPG substrate. The figure inset depicts an SEM micrograph of a CPG specimen.

will be shown below, channel throats rather than bulges are in control of both the condensation and evaporation threshold characteristics of CPG materials.

Figure 9 shows the nitrogen sorption isotherm at 76 K of the CPG substrate; the profile of this curve corresponds to a type IV isotherm (Sing *et al*. 1985) whilst its associated hysteresis loop is of type H1 shape. Tables 2 and 3 summarize some of the most important structural parameters of this glass sample. The nearly vertical slope of the DB curve demonstrates the relatively low dispersion of neck and cavity sizes existing along the channels of the CPG material. In turn, the upright slope of the AB isotherm suggests not only the existence of a narrow distribution of neck sizes, but also the presence of pore bulges connected to them. This seems to be the case; when capillary condensation starts occurring at pore throats, the liquid fronts created at such points advance systematically into the neighbouring cavities [this liquid transport is similar to the advanced adsorption situation shown in Figure 4(b)]. The possibility of liquid (condensate) percolation spreading throughout the entire network becomes greater and greater when the bulges become more and more similar in size to their interconnected bonds; under these circumstances, advancing liquid–vapour menisci can start trespassing into neighbouring cavities and bonds so that the AB curve becomes almost vertical.

In view of the above comments, it would seem appropriate to approximate the PSD determination for CPG materials in terms of a cylindrical pore arrangement. Consequently, the PSD function of the CPG substrate has been calculated from nitrogen/SiO_2 NLDFT kernels based on a cylindrical pore model. The narrowest cross-sections of the CPG channels may be imagined as types of tubular constrictions in which metastable (quasi-cylindrical) interfaces are developed on their surface during the early adsorption steps. Subsequently, with increasing vapour pressure, metastable films of an undulating character emerge on opposite sides of these channels and their eventual coalescence at their closest points of approach creates wedge-like menisci that commence invading subsequent pore channels with condensate. The flooding of the entire pore

TABLE 2. Pore Structural Properties of the CPG Solid as Determined by Nitrogen Sorption[a,b]

ε_{N_2}	A_{BET} (m^2/g)	A_t (m^2/g)	$V^P_{N_2}$ (mm^3/g)	V^{micro} (mm^3/g)	DB-PSD modes (nm)	DB-PSD mean (nm)	AB-PSD modes (nm)	AB-PSD mean (nm)
0.582	124	95	632	12	19.9, 16.3*	19.1 ± 0.9	19.7, 26.1†	18.9 ± 0.6

[a]Mean pore sizes were calculated by the NLDFT approach, the DB-BJH mode pore size being included for comparative purposes.

[b]ε_{N_2} = porosity from nitrogen sorption; A_{BET} = BET surface area; A_t = t surface area; $V^P_{N_2}$ = pore volume from nitrogen sorption; V^{micro} = micropore volume from t-plot. *DB-BJH mode pore size; † AB-BJH mode pore size.

TABLE 3. Pore Structural Properties of the CPG Solid According to Mercury Porosimetry[a] ($\theta = 135°$)

ε_{Hg}	A_{Hg} (m^2/g)	V^P_{Hg} (mm^3/g)	Hg-intr PSD mode (nm)	Hg-intr PSD mean (nm)	Hg-extr PSD mode (nm)	Hg-extr PSD mean (nm)
0.582	90	632	15.1	15 ± 0.6, 18.92 (166)	53.2, 19.1 (106)	53 ± 3.2

[a]ε_{Hg} = porosity from mercury intrusion; A_{Hg} = surface area from mercury intrusion; V^P_{Hg} = pore volume from mercury intrusion.

network in these CPG substrates is then achieved straightforwardly because the interconnected throats and cavities are similar in size. The desorption process from the liquid-saturated porous network commences as soon as percolating liquid–vapour menisci (corresponding to a wedge-like shape) are developed at the outer pore mouths; these interfaces immediately advance into the interior of the pore channels and thereby dislodge any condensate from them. Consequently, the widespread displacement of l–v menisci is very likely to be observed during capillary evaporation in CPG because of the similarity in size between the throats and their neighbouring cavities.

In the present work, PSD curves have been calculated from each of the AB and DB isotherms by employing (i) an NLDFT metastable kernel (applied to the AB curve) and (ii) an equilibrium NLDFT kernel (applied to the DB curve). The results of the NLDFT-PSD calculations are shown in Figure 10. It will be seen that since the AB and DB NLDFT-PSD curves look very similar to each other, the calculated mean pore diameters (Table 2) agree quite well, i.e. the NLDF metastable AB kernel has a value of 18.9 nm while the value for the equilibrium DB kernel is 19.1 nm. The agreement between the AB and DB NLDFT-PSD results clearly indicates that these CPG solids possess a type V structure where the interconnected throats and bulges are not too different in size and alternate with each other to form a pore channel system.

The above results suggest that hysteresis in the CPG solid arises from a combination of a *delay* in condensation at pore necks (i.e. instead of a stable wedge-like interphase, an undulating metastable shape is formed) and the subsequent movement of l–v menisci through successive cavities and throats. The straightforward displacement of menisci along the CPG channels during the condensation and evaporation processes explains the existence of a type H1 hysteresis loop. Consequently, the mechanism of pore condensation and evaporation in the CPG solid appears to be somewhat related to that in materials consisting of independent pores, since extensive sections of pores in the glass substrate are either filled with condensate or virtually emptied of condensate at a given vapour pressure. Accordingly, condensation and evaporation processes in CPG substrates involve percolation phenomena given the steep character of both the AB and DB isotherms as well as the widespread pore-to-pore displacement of liquid–gas menisci that occurs during these sorption processes.

Finally, it is interesting to note the following: (i) it is possible to deconvolute the AB-PSD profile into two constituting curves, the two AB-PSD peaks (see inset in Figure 10) which appear at 17.2 nm and 19.1 nm being indicative to some extent of the varying cross-sections of the CPG channels and (ii) the classical BJH-PSD adsorption and desorption curves are both biased towards smaller pore sizes relative to those obtained via the NLDFT treatment (see Figure 10), similar to the behaviour observed in some model pore systems such as SBA-15 or MCM-41.

4.2.2. Mercury porosimetry

Figure 11 shows the mercury intrusion/extrusion curves for the CPG sample. If the intrusion pressure threshold (i.e. 97 829 MPa) is related to the mean pore size obtained from the nitrogen NLDFT-DB curve (Table 2), the mean angle of inclination of the pore walls [calculated via equation (1)] is $\alpha_i = 31.3°$, provided the contact angle θ is 135°. A similar relationship occurs between the extrusion pressure threshold (i.e. 28 150 MPa) and the mean pore size obtained from the nitrogen NLDFT-AB isotherm, where an inclination angle $\alpha_r = -28.9°$ is calculated. Thus, the absolute values of the intrusion and extrusion inclination angles are close to each other, i.e. $|\alpha_i| \approx |\alpha_r|$, an observation which may be a reflection of the geometric characteristics of the homoclastic CPG surface. In addition to providing some vindication of the idea that the pore morphology in the CPG material can influence the PSD results, this approximate coincidence may also be a manifestation of a particular geometrical property of the CPG surface by reason of its presumably

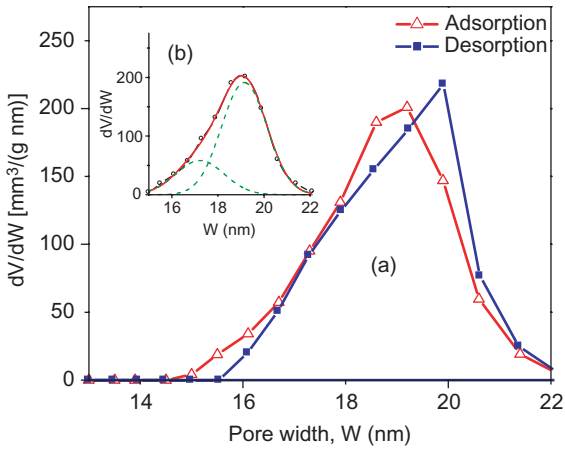

Figure 10. (a) AB-PSD (△) and DB-PSD (■) curves for the CPG substrate calculated from nitrogen sorption; (b) deconvolution of the AB-PSD curve (full line) into two subsidiary pore-size contributions (dashed lines).

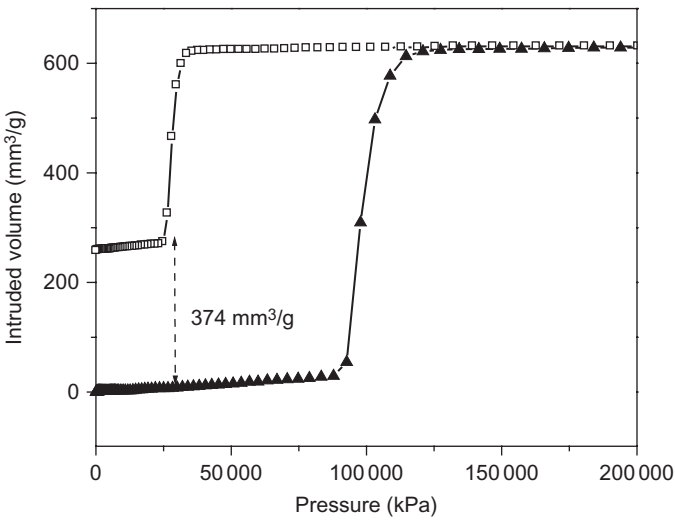

Figure 11. Mercury intrusion (▲)/extrusion (□) curves for the CPG sample.

constant curvature. From equation (3), it is possible to obtain the approximate site-to-bond size ratio R_S/R_B via the magnitude of the α_i and α_r angles, i.e. $R_S/R_B = 1.14$ for extrusion and $R_S/R_B = 1.17$ for intrusion. These size ratio values can be compared with the corresponding ratio obtained from the deconvolution of the NLDFT-AB PSD result into two contributory curves (see Figure 10), i.e. 19.1/17.2 = 1.11. Such results justify to some extent the idea that the sizes of the bulges and throats in the CPG substrate are not too different from each other.

These calculated values of the α_i and α_r angles lead to a reasonable match between the mean pore diameters obtained from mercury porosimetry and nitrogen sorption (see Figure 12 and the data listed in Tables 2 and 3), viz.18.9 nm (from mercury intrusion, with $\theta = 135°$ and $\alpha = 31.3°$)

versus 19.1 nm (from nitrogen desorption) and 19.1 nm (from mercury extrusion, with $\theta = 135°$ and $\alpha = -28.9°$) versus 18.9 nm (from nitrogen adsorption).

The BJH mean pore values arising from nitrogen sorption are 16.3 nm and 26.1 nm for the DB and the AB isotherms, respectively (Figure 12). Much of the discrepancy between mercury porosimetry and BJH pore sizes is probably due to the dissimilar θ values (i.e. 135° for intrusion, 0° for condensation) adopted by anchoring menisci along a sloping pore wall (cf. Section 2.3). Pore sizes obtained from nitrogen sorption (NLDFT) and mercury porosimetry (in the latter case, as long as α values are allowed for) are larger than the BJH desorption pore size since it is now well known (Mayagoitia 1993) that macroscopic (Kelvin) methods (such as BJH) under-estimate the void size quite appreciably. The under-estimation of pore sizes still persists with the NLDFT and BJH approaches, since (amongst other things) classical macroscopic, thermodynamic methods assume that the thermophysical properties of the confined fluid are the same as those in the bulk phase — which, of course, is not the case.

Assuming that the classical Washburn equation is applicable, mercury intrusion data for a substrate such as CPG should lead to smaller pore sizes than those provided by equation (1). This argument can be better explained in terms of equations (1) and (2) by assuming that, for the same experimental intrusion pressure P_i^I, two pore radii R_B and R_B' can arise depending as to whether the pore wall inclination angle α ($\alpha > 0^o$) is considered or not:

$$R_B = -\frac{2\sigma^{lv}\cos\theta}{P_i^I};\ R_B' = -\frac{2\sigma^{lv}\cos(\theta+\alpha)}{P_i^I};\ \therefore\ R_B < R_B' \tag{8}$$

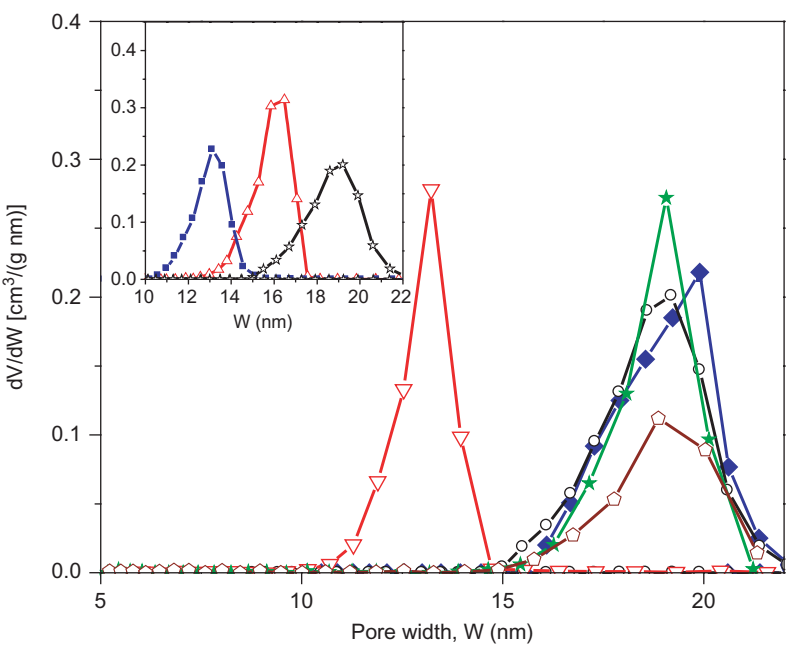

Figure 12. PSD results obtained for the CPG substrate. NLDFT-N_2 sorption results (○ AB, ◆ DB) are compared with PSD curves proceeding from (★) mercury intrusion taking place at $\Phi = 166^o$ ($\theta = 135°$, $\alpha = 31°$) and (▽) mercury intrusion taking place at $\Phi = 135^o$ ($\theta = 135°$, $\alpha = 0°$), and (⬠) mercury extrusion occurring at $\Phi = 106^o$ ($\theta = 135°$, $\alpha = 29°$). The inset depicts the classical BJH results: (■) N_2-BJH-AB; (△) N_2-BJH-DB; and (★) NLDFT-AB, with cylindrical condensation and hemispherical evaporation menisci being assumed in the latter calculation.

Hence, a disregard of the pore geometry during the analysis of mercury-intrusion data can certainly bring about an under-estimation of the pore size. On the other hand, mercury retraction treated via equation (1) usually leads to larger pore sizes than those obtained from the NLDFT method or even from the BJH treatment. This is because mercury extrusion in an undulating pore occurs at a pressure lower than that related to its widest cross-section through equation (1) (cf. Section 2.3). The mercury mode pore widths obtained from the Washburn equation [equation (1) assuming $\theta = 135°$] are 15.1 nm (intrusion) and 52.3 nm (extrusion). These two mode values are significantly different from the N_2-NLDFT results although satisfactory pore sizes can be obtained via equation (2) if an adequate value of Φ is assumed; once again, a disregard of the sloping nature of the CPG pore walls can greatly distort the mercury porosimetry PSD intrusion/extrusion outcomes.

It should be stated, however, that the fact that markedly different contact angles should be considered for advancing and receding menisci on solid surfaces is a well-documented phenomenon (Lowell and Shields 1981). In the present work, different intrusion and extrusion Φ ($= \theta + \alpha$) angles have been used to reconcile the nitrogen sorption and mercury porosimetry PSD results arising from a CPG substrate. Thus, the CPG-120 surface exhibits two threshold points at which mercury intrusion and extrusion occur in a percolative fashion; these points are located at inclination angles of $\alpha_i = 31.3°$ (intrusion) and $\alpha_r = -28.9°$ (extrusion).

Finally, and because of the somewhat extended mercury entrapment, it is very likely that mercury snap-off occurs at necks which are distributed isotropically throughout the network and which are surrounded by bulges (Rigby 2000). This latter supposition agrees with mercury porosimetry simulation experiments performed in model porous networks (Felipe 2005): these studies demonstrate that when the site connectivity is rather low (as would be expected in CPG substrates), snap-off at bonds takes place relatively easily, thus provoking the entrapment of mercury over a wide variety of cavity sizes all over the porous network.

5. CONCLUSIONS

Nitrogen sorption and mercury porosimetry involve a series of mechanistic aspects that determine the nature and extent of several irreversible and reversible processes occurring in porous media. Phenomena such as advanced and delayed adsorption in the case of nitrogen sorption, and canthotaxis and the effect of the orientation of pore walls on intrusion/extrusion thresholds in the case of mercury porosimetry, can be foreseen in model pore systems. In the present work, sorption and intrusion/extrusion experiments have been undertaken on two types of solids corresponding to extreme network morphologies in order to reach a critical assessment regarding the pore structural parameters obtained from experimental data proceeding from nitrogen sorption and mercury porosimetry measurements.

A rhombohedral lattice of monodisperse spherical particles of silica undergoes a progressive condensate filling that starts at pore windows (concurrently with the tetrahedral pores) and concludes at the octahedral holes. Mercury intrusion as well as nitrogen desorption are governed by the size of the triangular arrangements that delimit both the octahedral and tetrahedral pores of the spherical array. Mercury retraction is mostly limited by snap-off occurring at the pore windows surrounding the octahedral pores.

The porous structure of the CPG sample is a kind of manifold tubular system in which each channel consists of narrow zones that alternate with broader regions. Condensation at the narrower zones of the channels leads to immediate occupation by liquid flow of the subsequent site–throat

pairs. Throats also govern evaporation and mercury intrusion in the CPG sample, while the throat/cavity mean ratio of the void channels is a key factor determining the development of mercury retraction. Mercury intrusion and retraction data yield PSD sizes which are virtually identical to those arising from the NLDFT approach applied to nitrogen sorption, provided that the proper value is chosen for the angle of inclination of the pore walls. However, before mercury can permeate these voids, an intrusion threshold must be overcome somewhat beyond the entrances of pore bulges.

REFERENCES

Adamson, A.W. (1990) *Physical Chemistry of Surfaces*, Wiley, New York.

Aristov, B.G., Karnaukhov, A.P. and Kiselev, A.V. (1962) *Russ J. Phys. Chem.* **36,** 1159.

Barrett, E.P., Joyner, L.G. and Halenda, P.P. (1951) *J. Am. Chem. Soc.* **73,** 373.

Broekhoff, J.C.P. and de Boer, J.H. (1967) *J. Catal.* **9,** 8.

Cebeci, Ö.Z. (1980) *J. Colloid Interface Sci.* **78,** 383.

Cross, B.J. and Haynes, J.M. (1973) *Pore Structure and Properties of Materials*, Modry, S., Ed, Akademia, Prague, Czechoslovakia, Vol. 1, pp. C61–C69.

de Botton, S. (1985) *M.Sc. Thesis*, Universidad Autónoma Metropolitana-Iztapalapa, México City, México.

Domingues Dos Santos, F. and Ondarc, U.T. (1996) *J. Chim. Phys.* **93,** 1991.

Esparza, J.M., Ojeda, M.L., Campero, A., Domínguez, A., Kornhauser, I., Rojas, F., Vidales, A.M., López, R.H. and Zgrablich, G. (2004) *Colloids Surf. A* **241,** 35.

Everett, D.H. (1967) "Adsorption Hysteresis", in Flood, E.A., Ed, *The Solid–Gas Interface*, Marcel Dekker, New York, Vol. 2, pp. 1055–1113.

Everett, D.H. (1975) *J. Colloid Interface Sci.* **52,** 189.

Everett, D.H. and Haynes, J.M. (1975) *Z. Phys. Chem. (Frankfurt am Main)* **97,** 301.

Felipe, C. (2005) *Ph.D. Thesis*, Universidad Autónoma Metropolitana-Iztapalapa, México City, México.

Gelb, L.D. and Gubbins, K.E. (2000a) *Studies in Surface Science and Catalysis,* Unger, K.K., Kreysa, G., Baselt, J.P., Eds, Vol. 128, Elsevier, Amsterdam, Vol. 128, pp. 61–69.

Gelb, L.D. and Gubbins, K.E. (2000b) *Fundamentals of Adsorption 6,* Meunier, F., Ed, Elsevier, Amsterdam, pp. 551–556.

Graton, L.C. and Fraser, N.J. (1935) *J. Geol.* **43,** 785.

Lam, C.N.C., Ko, R.H.Y., Yu, L.M.Y., Ng, A., Li, D., Hair, M.L. and Neumann, A.W. (2001) *J. Colloid Interface Sci.* **243,** 208.

Lowell, S. and Shields, J.E. (1981) *J. Colloid Interface Sci.* **80,** 192.

Lukens, W.W., Schmidt-Winkel, P., Zhao, D., Feng, J. and Stucky, G.D. (1999) *Langmuir* **15,** 5403.

Martinez, I., Haynes, J.M. and Langbein, D. (1987) "Fluid Statics and Capillarity", in *Fluids and Material Sciences in Space*, Walter, H.U., Ed, Springer-Verlag, Berlin, pp. 53–80.

Mayagoitia, V. (1993) *Catal. Lett.* **22,** 93.

Mayagoitia, V., Rojas, F. and Kornhauser, I. (1985) *J. Chem. Soc., Faraday Trans.* **81,** 2931.

Neimark, A.V. and Ravikovitch, P.I. (2001) *Microporous Mesoporous Mater.* **44/45,** 697.

Neimark, A.V. and Ravikovitch, P.I. (2003) *J. Phys., Condens. Mater.* **15,** 347.

Ojeda, M.L., Esparza, J.M., Campero, A., Cordero, S., Kornhauser, I. and Rojas, F. (2003) *Phys. Chem. Chem. Phys.* **5,** 1859.

Ravikovitch, P.I. and Neimark, A.V. (2001) *J. Phys. Chem. B* **105,** 6817.

Ravikovitch, P.I. and Neimark, A.V. (2002) *Langmuir* **18,** 1550.

Ravikovitch, P.I., Haller, G.L. and Neimark, A.V. (1998) *Adv. Colloid Interface Sci.* **76/77,** 203.

Reyes-de la Cruz, M.R. (1979) *M.Sc. Thesis*, Universidad Autónoma Metropolitana-Iztapalapa, México City, México.

Rigby, S.P.J. (2000) *J. Colloid Interface Sci.* **224,** 382.

Ritter, H.L. and Drake, L.C. (1945) *Ind. Eng. Chem., Anal. Ed.* **17,** 782.
Salmas, C. and Androutsopoulos, G. (2001) *J. Colloid Interface Sci.* **239,** 178.
Sarkisov, L. and Monson, P.A. (2001) *Langmuir* **17,** 7600.
Scherer, G.W. (1998) *Adv. Colloid Interface Sci.* **76/77,** 321.
Sing, K.S.W. (1998) *Adv. Colloid Interface Sci.* **76/77,** 3.
Sing, K.S.W., Everett, D.H., Haul, R.A., Moscou, L., Pierotti, R.A., Rouquérol, J. and Siemieniewska, T. (1985) *Pure Appl. Chem.* **57,** 603.
Tsakiroglou, D., Kolonis, G.B., Roumeliotis, T.C. and Payatakes, A.C. (1997) *J. Colloid Interface Sci.* **193,** 259.
Washburn, E.W. (1921) *Phys. Rev.* **17,** 273.
Zhao, D., Feng, J., Huo, Q., Melosh, N., Fredrickson, G.H., Chmelka, B.F. and Stucky, G.D. (1998a) *Science* **279,** 548.
Zhao, D., Huo, Q., Feng, J., Chmelka, B.F. and Stucky, G.D. (1998b) *J. Am. Chem. Soc.* **120,** 6024.